Accepted Manuscript

Title: Beam-induced oxidation of mixed-valent Fe (oxyhydr)oxides (green rust) monitored by STEM-EELS

Authors: H.M. Freeman, J.P.H Perez, N. Hondow, L.G. Benning, A.P. Brown

Please cite this article as: Freeman HM, Perez JPH, Hondow N, Benning LG, Brown AP, Beam-induced oxidation of mixed-valent Fe (oxyhydr)oxides (green rust) monitored by STEM-EELS, *Micron* (2019), https://doi.org/10.1016/j.micron.2019.02.002

Beam-induced oxidation of mixed-valent Fe (oxyhydr)oxides (green rust) monitored by STEM-EELS

H.M.Freeman[1,2], J.P.H Perez[1,3], N. Hondow[2], L.G. Benning[1,3,4], A.P. Brown[2].

[1]GFZ German Research Center for Geosciences, Telegrafenberg, 14473 Potsdam, Germany

[2]School of Chemical and Process Engineering, University of Leeds, Leeds, LS2 9JT, United Kingdom

[3]Department of Earth Sciences, Free University of Berlin, 12249 Berlin, Germany

[4]School of Earth and Environment, University of Leeds, Leeds, LS2 9JT, United Kingdom

HIGHLIGHTS:

- Energy resolved STEM-EELS to quantify Fe oxidation states in green rust

- Demonstration of electron beam induced in-situ oxidation

- Methodology for quantifying the interaction between green rust and toxic metals

Abstract

Analytical transmission electron microscopy (TEM) is often used to investigate morphologies, crystal structures, chemical compositions and oxidation states of highly reactive mixed-valent mineral phases. Of prime interest, due to its potential role in toxic metal remediation, is green rust sulphate (GR_{SO4}) an Fe^{II}-Fe^{III} layered double hydroxide. In this study, we quantified the effects that TEM analysis has on GR_{SO4} in order to ensure the measured material properties are a result of synthesis and reaction kinetics, and not due to sample preparation and analysis technique. To do this, we compared

two sample preparation techniques (anoxic drop-cast with drying, and frozen-hydrated cryogenic) and exposed samples to the electron beam for several minutes, acquiring fluence series between ca. 40 e⁻ Å⁻² and 10,000 e⁻Å⁻². TEM imaging and electron diffraction showed that the hexagonal plate-like morphology and crystal structure of GR_{SO4} were largely unaffected by sample preparation and analysis technique. However, quantitative analysis of a series of monochromated Fe $L_{3,2}$-edge electron energy loss spectra (EELS) showed that electron irradiation induces oxidation. We measured an Fe(II)/Fe(III) ratio of 1.94 (as expected for GR_{SO4}) at 50 e⁻Å⁻² . However, above this fluence, the ratio logarithmically decreased and dropped to ca. 0.5 after 1000 e⁻Å⁻². This trend was approximately the same for both sample preparation techniques implying that it is the beam alone which causes valence state changes, and not exposure to oxygen during transfer into the TEM or the vacuum of the TEM column. Ultimately this work demonstrates that GR valence can be quantified by EELS provided that the sample is not over exposed to electrons. This also opens the possibility of quantifying the effect of redox-sensitive toxic metals (e.g., As, Cr, Se) on Fe oxidation state in GR phases (relevant to the treatment of contaminated soils and water) with a higher spatial resolution than other techniques (e.g., Mössbauer spectroscopy).

KEYWORDS: monochromated EELS; Fe oxidation; green rust; cryo-TEM; low dose TEM.

1. Introduction

Green rust (GR) materials are redox-active, mixed-valent Fe(II)-Fe(III) layered double hydroxides which exhibit high surfaces area and can intercalate inorganic or organic species into the plate-like structure due to their anion exchange capacity (Goh et al., 2008; Newman and Jones, 1998; Usman et al., 2018). GR phases can be easily engineered for a wide-range of applications such as catalysis, electrochemistry, and environmental remediation (Bhave and Shejwalkar, 2018; Chen et al., 2018; Huang et al., 2019; Zhang et al., 2018). In particular, they are promising reactants for ground water remediation where they have been shown to remove toxic metal contaminants from water by adsorption (Jönsson and Sherman, 2008; Mitsunobu et al., 2009; Perez et al., 2019), reduction (O'Loughlin et al.,

2003; Skovbjerg et al., 2006; Thomas et al., 2018), interlayer intercalation (Refait et al., 2000) and substitution of structural Fe (Ahmed et al., 2008; Refait et al., 1990).

Green rust sulphate ($[NaFe^{II}_6Fe^{III}_3(OH)_{18}(SO_4)_2\cdot12H_2O]$ hereafter referred to as GR_{SO4}) is composed of positively charged brucite-like iron hydroxide layers that alternate with interlayers containing sulphate and water molecules (following Christiansen et al.). The structural Fe(II)/Fe(III) ratio of 2 has been determined by Mössbauer spectroscopy, chemical analysis, and X-ray diffraction (Christiansen et al., 2009; Génin et al., 1996; Hansen et al., 1994; Perez et al., 2019; Refait et al., 1999, 1990). When using GR for groundwater remediation, it is important the mineral remains stable and does not transform to other iron (oxyhydr)oxides, which can be less effective substrates for the sequestration of toxic metals. For example, partial oxidation or transformation of GR phases to other iron (oxyhydr)oxides can lessen its ability to reduce redox-sensitive metals (e.g. Cr, Se, U) or its adsorption uptake (e.g. As) (Jönsson and Sherman, 2008; O'Loughlin et al., 2003; Perez et al., 2019; Skovbjerg et al., 2006; Thomas et al., 2018). One way to check the stability of GR over time is to monitor the Fe(II)/Fe(III) ratio following interaction with metals. As such, it is essential that applied characterisation techniques can quantitatively evaluate any changes in oxidation state resulting from environmental reactions and are not a result of the characterization technique itself. Analytical transmission electron microscopy (TEM) provides information at high spatial resolution regarding the morphology, crystal structure, chemical composition and oxidation state of a specimen. To date, many TEM studies of GR have used conventional sample preparation techniques (drop-cast and dried) under anoxic conditions (Ahmed et al., 2010; Bach et al., 2014; Géhin et al., 2002; Mann et al., 1989; Perez et al., 2019; Skovbjerg et al., 2006; Thomas et al., 2018). Such methods involve aqueous sample dilution, drop casting onto a TEM grid and drying with alcohol in an anaerobic chamber to minimise the risk of oxidation. The dried grid thus contains a well dispersed sample that is subsequently exposed to air for rapid transfer into the TEM. Much of the literature regarding TEM of GR has so far assumed that both sample preparation and the TEM environment do not significantly affect the specimen. In some studies (particularly Johnson et al. (2015)) these factors are taken into account, such as the short term air exposure during sample transfer to the TEM and electron beam induced "nanoscale restructuring", where low dose

operating conditions were used (Johnson et al., 2015). Here, we further explore these factors in relation to the stability of the oxidation state by measuring electron energy loss spectra (EELS) at the valence sensitive Fe $L_{3,2}$-edge following both conventional (anoxic drop-cast and dried) and cryogenic (cryo; frozen hydrated suspension) sample preparation for a range of controlled electron fluences.

Minimising exposure of GR to oxygen prior to TEM analysis and to vacuum dehydration during TEM analysis can be achieved by retaining the mineral in a thin layer of vitreous ice; the grid must be wetted, blotted and plunge frozen into liquid ethane for cryo transfer into the TEM. This method results in the GR plates being dispersed in a thin layer of electron transparent, vitreous ice. Cryo-TEM has been successfully used to investigate the formation of magnetite (Fe_3O_4) from a ferrihydrite precursor, which can often proceed via GR as a transient phase, a process that had previously only been quantified by time resolved X-ray diffraction (Dey et al., 2015; Michel et al., 2010; Sumoondur et al., 2008). The cryo-TEM sample preparation used by Dey et al. (2015) was required to capture and monitor the morphological changes of the gel-like ferrihydrite precursor phase at various points during the transformation reaction.

Assessing a specimen's sensitivity to electron irradiation can be achieved by collecting an electron fluence series whereby the same area is repeatedly analysed during exposure to the electron beam. Knowledge of the beam current, size of the analysed area, and the time the specimen is exposed to the beam allows for the number of electrons per unit area (i.e. fluence) to be determined. A critical fluence can then be calculated when the property being measured changes by a characteristic value (e.g., 1/e). Previous TEM studies of Fe-bearing minerals have used EELS to show that electron irradiation can induce changes in the oxidation state of structural Fe (Garvie et al., 2004; Pan et al., 2010). In the work of Garvie et al. (2004), a threshold fluence of 10^4 e$^-$Å^{-2} (for a 100 kV beam) was determined for the iron silicate mineral cronstedtite ($Fe^{II}_2Fe^{III}(SiFe^{III}O_5)(OH)_4$). It was found that beyond this fluence, the electron beam-induced loss of structural H in the specimen was likely to be significant enough to cause oxidation, as measured by an increasing Fe(III) contribution to the EELS Fe $L_{3,2}$-edge. It was also demonstrated that thinner specimens (< 400 Å) were more susceptible to beam-induced alterations. Conversely, 200 kV EELS analysis at the Fe L_3-edge by Pan et al. (2010) showed a reduction in Fe(III)

content following electron irradiation of various Fe-bearing phases (iron phosphate dihydrate, ferrihydrite, haemosiderin and ferritin). They proposed that the dominant damage mechanism was radiolysis induced loss of structural O, OH and H_2O, resulting in both Fe coordination and oxidation state changes. In addition, the hydrated samples were found to be more beam sensitive than cronstedtite (reported by Garvie et al. 2004), potentially due to increased levels of H_2O associated with these minerals increasing the efficiency of radiolysis.

The work reported here used analytical (S)TEM including imaging, selected area electron diffraction (SAED) and monochromated EELS to monitor changes in morphology, crystal structure and Fe(II)/Fe(III) ratio of GR_{SO4} plates that were prepared through two different TEM sample preparation techniques: (i) drop-cast onto TEM grids and dried (in anoxic atmosphere, with rapid air transfer to the TEM) and (ii) frozen hydrated suspensions cryo-transferred and cryo-analysed. This allowed us to isolate the factors which we hypothesised might contribute to a change in oxidation state: (i) exposure to oxygen during TEM transfer of anoxic drop-cast and dried samples (potentially sufficient to oxidise the sample); (ii) exposure to the vacuum in the microscope column (potentially sufficient to cause loss of interlayer water molecules and associated sulphate groups in the A, B planes which may lead to a change in the interlayer charge balance, increasing Fe(III) content (Simon et al., 2003)); and (iii) exposure to electron irradiation (potentially sufficient to either induce a loss of structural H and oxidise the specimen (Garvie et al., 2004), or induce radiolysis and reduce the specimen (Pan et al., 2010)).

In this work, we revisit similar Fe $L_{3,2}$-edge analysis methods to those used by Pan et al. (2010), but with the improved energy resolution of a monochromated electron source and additional, absolute edge energy measurement by dual EELS acquisition (Gubbens et al., 2010). In addition, we demonstrate the need for low fluence EELS in order to measure representative Fe(II)/Fe(III) ratios for GR_{SO4} at a higher spatial and energy resolution than previously reported techniques (Génin et al., 1996; Hansen et al., 1994; Perez et al., 2019; Refait et al., 1999, 1990).

2. Materials and Methods

GR with interlayer sulphate was synthesized in aqueous suspension in an anaerobic chamber (97% N_2, 3% H_2, Coy Laboratory Products, Inc.) at room temperature using a modified co-precipitation method

5

(Géhin et al., 2002; Perez et al., 2019). We ensured the supernatant used in the sample preparation steps did not contain excess Fe^{2+} from the initial synthesis, as this would have added to the EELS signal. To achieve this, the fresh GR_{SO4} slurry was rinsed inside the anaerobic chamber with de-oxygenated deionized water by centrifugation and re-dispersion until the Fe^{2+} concentration in the supernatant was below 2 mM (as measured by inductively coupled plasma - optical emission spectrometry (ICP-OES)). All drop-cast TEM sample preparation was performed in the anaerobic chamber using diluted suspensions in de-oxygenated water. These diluted suspensions were drop cast onto holey amorphous carbon Cu grids (Agar Scientific Ltd.), left to dry in the anaerobic chamber and further dehydrated with a drop of ethanol. Samples were transferred to the TEM in a grid box wrapped in parafilm, loaded into a double tilt FEI TEM holder and inserted into the TEM; the grid was exposed to air for approximately 60 s. In all cases, data was collected from clean GR plates; those that were considered free of contamination and/or visible stray iron (oxyhydr)oxide minerals of different valence ratios.

Cryo TEM sample preparation used non-diluted suspensions. Approximately 3.5 μL was dispensed by micro pipette onto a lacey amorphous carbon coated Cu grid which was blotted and plunge frozen into liquid ethane by an FEI Vitrobot© markIV (at blot force 6). The undiluted suspension was exposed to air at 100% humidity for less than 5 s before plunge freezing. The frozen sample was then cryo-transferred into the TEM using a Gatan 914 holder with the temperature maintained below -165 °C.

For both sample preparation techniques, an FEI Titan[3] Themis G2 S/TEM operating at 300 kV was used with an FEI Super-X energy dispersive X-ray (EDX) system, a monochromator with an energy spread of ca. 0.35 eV, a Gatan Quantum 965 ER energy filter for dual EELS (which allows for core-loss edges to be calibrated against the simultaneously acquired low loss spectrum) and a Gatan OneView CCD. A ca. 1.4 Å probe was formed for STEM with an estimated convergence semi-angle of ca. 10 mrad (limited by the second smallest C3 aperture) and a probe current of up to 300 pA when the monochromator is excited (as measured by the dose metre on the flu cam, calibrated using a Faraday cup). Fluence was controlled in STEM by limiting the dwell time (to as low as 0.8 μs) and pixel size and collecting EEL spectra while scanning (i.e. by continuously scanning at a magnification that approximately matches the GR plate size to the field of view). In STEM-EELS mode, a 2.5 mm

entrance aperture provided a collection semi-angle of 21 mrad. Spectra were collected for 30 s and then background subtracted (power law) in 'Gatan Microscopy Suite' software (version 3.0.1), with t/λ values generally < 0.35 for anoxic drop-cast specimens. SAED patterns were obtained using an aperture with an effective diameter of 200 nm at the imaging plane. The electron fluence per frame (F) was calculated using equation 1:

$$F(e^-\text{Å}^{-2}) = \frac{I \times t}{e^- \times d_s^2}$$ Eq. 1

Where t is the dwell time, I is the probe current, e^- is the charge of an electron (1.602×10^{-19} C) and d_s is the pixel size.

3. Results

TEM images showed hexagonal GR_{SO4} plates between 0.1-1 μm in width, and ca. 20-50 nm thick (as measured from the low loss EEL spectrum) (Figure 1). The general morphology of the GR plates did not vary between sample preparation technique, and the SAED patterns provide evidence that the hexagonal crystal structure was maintained. EDX spectroscopy (not shown) confirmed the presence of Fe, S and O as expected. Diffraction patterns from both sample preparation techniques show reflections for the {300} and {330} family of spots which are at 2.77 Å and 1.60 Å respectively and close in value to those reported by powder XRD (2.75 Å and 1.59 Å) (Christiansen et al., 2009). Diffraction patterns collected at higher fluences (>10,000 e⁻Å⁻²) showed slightly lower in-plane atomic spacing values for the same type of pattern, of 2.59 Å {300} and 1.51 Å {330}, a reduction of 6% for both planes.

To measure the effect of electron irradiation on oxidation state, EELS Fe $L_{3,2}$-edges were collected at known fluences and compared to reference spectra; Figure 2 shows representative low fluence spectra from both sample preparation techniques and the reference materials. To date, techniques to quantify the Fe(II)/Fe(III) ratio in Fe bearing materials via EELS have used $L_{3,2}$-edges for the white line intensity ratio method (Cavé et al., 2006; Van Aken and Liebscher, 2002), have included the O-K edge (Brown et al., 2001), or used reference spectra for non-linear least-squares (NLLS) fitting (Pan et al., 2009, 2006, 2010). With recent advances in EELS energy resolution via the addition of a monochromator or the use of a cold FEG (Paterson and Krivanek, 1990), it is now possible to clearly resolve two sub-

peaks within the Fe L_3 edge; the lower energy sub-peak at ca. 709.0 eV can be attributed to a predominant Fe^{2+} contribution and the higher energy sub-peak at ca. 710.8 eV to a Fe^{3+} contribution (Brown et al., 2017). Being able to resolve these two sub-peaks enables a more accurate multiple linear least-square (MLLS) fitting, and a ratio of Fe(II)/Fe(III) to be calculated. In this work, we fitted the acquired Fe $L_{3,2}$-edges against reference spectra of hedenbergite (100% octahedral Fe^{2+}) and haematite (100% octahedral Fe^{3+}) using the 'Gatan Microscopy Suite' software (Figure 3). The higher energy sub-peak of the core loss spectra were energy calibrated to 710.8 eV, background subtracted and area normalised in the energy range 702-730 eV before being fitted. The spectra of the reference material were collected with the same TEM and the same monochromator excitation but under the TEM collection conditions described in Brown et al. (2017).

Applying this fitting procedure to spectral series from both sample preparation techniques provides quantitative evidence for the *in-situ* oxidation of GR_{SO4} during exposure to the electron beam. Stacked spectral series (along with the MLLS fits) for both the cryo-frozen hydrated GR_{SO4} and the anoxic drop-cast sample preparation methods are shown in Figure 4, and the measured change in Fe(II)/Fe(III) ratio with electron fluence is plotted in Figure 5 (for both sample preparation techniques). Figure 4 shows how the relative intensities of the two sub-peaks in the Fe-L_3 edge change with electron fluence; the intensity of the 709.0 eV peak quickly diminishes for both datasets. By ca. 1000 $e^-Å^{-2}$ the relative intensities of the two peaks tend not to change further for the cryo data whereas the 709.0 eV peak continues to reduce for the drop-cast data. Following quantification of these peaks with the MLLS fitting procedure, it is possible to calculate that for the cryo data the Fe(II)/Fe(III) ratio stabilises at around 0.5 after ca. 1000 $e^-Å^{-2}$, and for the drop-cast data it stabilises at 0.15 after 6000 $e^-Å^{-2}$ (Figure 5). The initial Fe(II)/Fe(III) ratio was higher for drop-cast samples (ca. 1.93) as it was possible to collect spectra with sufficient signal to noise ratios at a lower fluence due to the lack of vitreous-ice.

Trendlines have been added to the data series in Figure 5 to measure the gradient (i.e., the rate of oxidation with electron fluence) and to extrapolate the data to the theoretical Fe(II)/Fe(III) ratio (2 for GR_{SO4}). These extrapolated trendlines for both sample preparation techniques essentially meet at

8

Fe(II)/Fe(III) = 2 as might be expected. This allowed us to determine a threshold fluence of 40 ± 5 e⁻Å⁻², beyond which electron beam-induced oxidation occurred with either preparation method.

4. Discussion

We can now address the key factors which we initially hypothesised might contribute to a change in oxidation state of GR when measured by (S)TEM-EELS. We have demonstrated that exposure to oxygen during TEM transfer of the anoxic drop-cast and dried samples was not sufficient to cause discernible oxidation because the measured Fe(II)/Fe(III) ratio (as high as 1.93 ± 0.09) was retained at low fluences. In addition, we can exclude the hypothesis that exposure to the vacuum in the electron column was sufficient to cause loss of interlayer water molecules and associated sulphate groups which may have led to a charge imbalance, as we have observed similar trends from both anoxic drop-cast samples and cryo frozen-hydrated samples, the latter of which is not directly exposed to the vacuum. The third hypothesis regarding electron irradiation induced valence changes has also been addressed and we showed that there is a threshold fluence of 40 ± 5 e⁻Å⁻² for the onset of GR oxidation for either specimen preparation route. Unfortunately, collecting EELS spectra at such a low fluence is challenging and we have compromised spatial resolution to approximately the size of an individual GR plate in order to approach these values. Above this fluence threshold, we saw progressive oxidation of the GR for anoxic drop-cast samples, where exposure to electron irradiation was sufficient to induce the deprotonation of apical OH⁻ ions in the Fe octahedra (i.e. loss of structural H as reported by *Garvie et al.* (2004) for mixed-valent Fe-bearing silicates). This charge imbalance within the Fe hydroxide layer is compensated through the oxidation of structural Fe(II) to Fe(III). The *in situ* oxidation of GR phases through deprotonation of the apical OH⁻ ions has been previously studied in GR carbonate by Mössbauer spectroscopy and X-ray photoelectron spectroscopy (Ruby et al., 2006; Genin et al., 2006; Ruby et al., 2008; Mullet et al., 2008). For cryo frozen-hydrated samples, this also seems to be the case for relatively low fluences (i.e. <1000 e⁻Å⁻²), however beyond this point, the Fe(II)/Fe(III) content apparently stabilises at 0.5. At fluence values above 1000 e⁻Å⁻² the vitreous ice (encasing the GR plates) has been shown to melt and or sublime (Ilett et al., 2019) and certainly by this stage diffusion limited damage due to the beam-induced radiolysis of the ice will become significant so that H₂O loss and reduction (as

reported by Pan et al. 2010) might operate alongside the ongoing beam-induced oxidation (as reported by Garvie et al. (2004) and documented in this study). The fact that the Fe(II)/Fe(III) ratio plateaus at a value of ca. 0.5 suggests that together, these mechanisms have a balanced effect which does not alter the net oxidation state (Figure 5).

The subtle differences between in-plane atomic spacings measured by SAED for low (< 1000 e$^-$Å^{-2}) and high ($> 10,000$ e$^-$Å^{-2}) fluences could also be evidence for beam-induced oxidation. Calculations by Shannon (1976) showed that the ionic radius of Fe depends on its oxidation state; 0.780 Å in Fe(II) and 0.645 Å in Fe(III), which corresponds to a 17 % reduction in ionic radius following complete oxidation (Shannon, 1976). While dehydration of the sample (in the TEM high vacuum column) would also decrease d-spacing, this reduction would only occur between iron hydroxide layers and not in-plane. The measured fluence dependent reduction of in-plane atomic spacings in this study might therefore be attributed to the partial oxidation of Fe although further investigation, collecting a fluence series of SAED patterns, would be needed to confirm this. If confirmed, this method could be used to monitor GR oxidation on TEMs which do not have the ability to acquire high resolution monochromated EELS.

Ultimately, with this work we have demonstrated that only by using low fluences can one obtain truly representative Fe(II)/Fe(III) ratios in GR when analysing these redox sensitive materials by STEM-EELS. Spatial resolution has been compromised to achieve this however smart acquisition techniques such as that reported by Sader et al. (2010) may be used to improve spatial resolution and assess valence variation across an individual GR plate (Sader et al., 2010). This technique relies on averaging spectra from the same position within multiple plates to increase EELS signal and improve spatial resolution while minimising net fluence.

5. Conclusion

We have studied GR$_{SO4}$ using analytical TEM, in particular monochromated STEM-EELS, to demonstrate the sensitivity of Fe(II) content under electron irradiation. Using anoxic drop-casting and cryogenic sample preparation techniques allowed us to isolate the cause of oxidation to structural H loss induced by the electron beam, and not exposure to oxygen during sample transfer into the TEM or to the vacuum within the TEM column. MLLS fitting to reference Fe L_3-edge EEL spectra enabled

10

the Fe(II)/Fe(III) ratio to be determined which was plotted against electron fluence to identify the beam induced oxidation rate. The lowest fluence Fe(II)/Fe(III) ratio was 1.93 ± 0.09 at 40 e$^-$Å^{-2} and compares favourably with the expected value of 2. Beam induced *in-situ* oxidation of GR$_{SO4}$ was quantified for both sample preparation techniques allowing us to calculate a threshold fluence at which oxidation begins (40 e$^-$Å^{-2}), and at which the Fe(II)/Fe(III) ratio stabilises at 0.15 for anoxic drop-cast samples (6000 e$^-$Å^{-2}) and 0.5 for cryo-samples (at ca. 1000 e$^-$Å^{-2}). Based on these results we have developed a robust analytical TEM methodology for the investigation of highly redox sensitive materials like GR. This low fluence approach can be applied to measure the spatial variation in Fe(II) content across a single GR plate and to measure change in Fe(II) content of GR reacted with toxic metals such as As, Cr and Se (relevant to the remediation of polluted water).

6. Acknowledgments

References

Ahmed, I.A.M., Benning, L.G., Kakonyi, G., Sumoondur, A.D., Terrill, N.J., Shaw, S., 2010. Formation of Green Rust Sulfate : A Combined in Situ Time-Resolved X-ray Scattering and Electrochemical Study 26, 6593–6603. https://doi.org/10.1021/la903935j

Ahmed, I.A.M., Shaw, S., Benning, L.G., 2008. Formation of hydroxysulphate and hydroxycarbonate green rusts in the presence of zinc using time-resolved in situ small and wide angle X-ray scattering. Mineral. Mag. 72, 159–162. https://doi.org/10.1180/minmag.2008.072.1.159

Bach, D., Christiansen, B.C., Schild, D., Geckeis, H., 2014. TEM study of Green Rust Sodium Sulphate (GR Na , SO4) Interacted with Neptunyl Ions (NpO 2 +) 102, 279–289. https://doi.org/10.1515/ract-2013-2105

Bhave, C., Shejwalkar, S., 2018. A review on the synthesis and applications of green rust for environmental pollutant remediation. Int. J. Environ. Sci. Technol. 15, 1243–1248. https://doi.org/10.1007/s13762-017-1468-y

Brown, A.P., Hillier, S., Brydson, R.M.D., 2017. Quantification of Fe-oxidation state in mixed valence minerals: a geochemical application of EELS revisited. J. Phys. Conf. Ser. 902, 012016.

https://doi.org/10.1088/1742-6596/902/1/012016

Brown, A.P., Moore, R.G.C., Evans, S.D., Brydson, R., 2001. Characterisation of Iron Oxide Nanoparticles Using EELS. J. Phys. Conf. Ser. 168, 255–258.

Cavé, L., Al, T., Loomer, D., Cogswell, S., Weaver, L., 2006. A STEM/EELS method for mapping iron valence ratios in oxide minerals. Micron 37, 301–309. https://doi.org/10.1016/j.micron.2005.10.006

Chen, Y., Gao, S., Liu, Z., Shao, S., Yin, W., Fang, Z., Huang, L.-Z., 2018. Prolonged persulfate activation by UV irradiation of green rust for the degradation of organic pollutants. Environ. Chem. Lett. https://doi.org/10.1007/s10311-018-0815-7

Christiansen, B.C., Balic-Zunic, T., Petit, P.O., Frandsen, C., Mørup, S., Geckeis, H., Katerinopoulou, A., Stipp, S.L.S., 2009. Composition and structure of an iron-bearing, layered double hydroxide (LDH) - Green rust sodium sulphate. Geochim. Cosmochim. Acta 73, 3579–3592. https://doi.org/10.1016/j.gca.2009.03.032

Dey, A., Lenders, J.J.M., Sommerdijk, N.A.J.M., 2015. Bioinspired magnetite formation from a disordered ferrihydrite-derived precursor. Faraday Discuss. 179, 215–225. https://doi.org/10.1039/C4FD00227J

Garvie, L.A.J., Zega, T.J., Rez, P., Buseck, P.R., 2004. Nanometer-scale measurements of Fe 3 + / ΣFe by electron energy-loss spectroscopy : A cautionary note. Am. Mineral. 89, 1610–1616.

Géhin, A., Ruby, C., Abdelmoula, M., Benali, O., Ghanbaja, J., 2002. Synthesis of Fe (II-III) hydroxysulphate green rust by coprecipitation. Solid State Sci. 4, 61–66.

Génin, J.M.R., Olowe, A.A., Refait, P., Simon, L., 1996. On the stoichiometry and pourbaix diagram of Fe(II)-Fe(III) hydroxy-sulphate or sulphate-containing green rust 2: An electrochemical and mössbauer spectroscopy study. Corros. Sci. 38, 1751–1762. https://doi.org/10.1016/S0010-938X(96)00072-8

Goh, K.H., Lim, T.T., Dong, Z., 2008. Application of layered double hydroxides for removal of oxyanions: A review. Water Res. 42, 1343–1368. https://doi.org/10.1016/j.watres.2007.10.043

Gubbens, A., Barfels, M., Trevor, C., Twesten, R., Mooney, P., Thomas, P., Menon, N., Kraus, B., Mao, C., McGinn, B., 2010. The GIF Quantum, a next generation post-column imaging energy filter. Ultramicroscopy 110, 962–970. https://doi.org/10.1016/j.ultramic.2010.01.009

Hansen, H.C.B., Borggaard, O.K., Sørensen, J., 1994. Evaluation of the free energy of formation of Fe(II)-Fe(III) hydroxide-sulphate (green rust) and its reduction of nitrite. Geochim. Cosmochim. Acta 58, 2599–2608. https://doi.org/10.1016/0016-7037(94)90131-7

Huang, L.-Z., Zhu, M., Liu, Z., Wang, Z., Hansen, H.C.B., 2019. Single sheet iron oxide: An efficient heterogeneous electro-Fenton catalyst at neutral pH. J. Hazard. Mater. 364, 39–47. https://doi.org/10.1016/j.jhazmat.2018.10.026

Ilett, M., Brydson, R., Brown, A., Hondow, N., 2019. Cryo-analytical STEM of frozen, aqueous dispersions of nanoparticles. Micron Submitted.

Johnson, C.A., Murayama, M., Küsel, K., Hochella, M.F., 2015. Polycrystallinity of green rust minerals and their synthetic analogs : Implications for particle formation and reactivity in complex systems. Am. Mineral. 100, 2091–2105. https://doi.org/10.2138/am-2015-5287

Jönsson, J., Sherman, D.M., 2008. Sorption of As(III) and As(V) to siderite, green rust (fougerite) and magnetite: Implications for arsenic release in anoxic groundwaters. Chem. Geol. 255, 173–181. https://doi.org/10.1016/j.chemgeo.2008.06.036

Mann, S., Sparks, N.H.C., Couling, S.B., Larcombe, M.C., Frankel, R.B., 1989. Crystallochemical Characterization of Magnetic Spinels prepared from Aqueous Solution. J. Chem. Soc. Faraday

Trans. 1 Phys. Chem. Condens. Phases 85, 3033–3044. https://doi.org/10.1039/F19898503033

Michel, F.M., Barron, V., Torrent, J., Morales, M.P., Serna, C.J., Boily, J.-F., Liu, Q., Ambrosini, A., Cismasu, A.C., Brown, G.E., 2010. Ordered ferrimagnetic form of ferrihydrite reveals links among structure, composition, and magnetism. Proc. Natl. Acad. Sci. 107, 2787–2792. https://doi.org/10.1073/pnas.0910170107

Mitsunobu, S., Takahashi, Y., Sakai, Y., Inumaru, K., 2009. Interaction of synthetic sulfate green rust with antimony(V). Environ. Sci. Technol. 43, 318–323. https://doi.org/10.1021/es8026067

Newman, S.P., Jones, W., 1998. Synthesis , characterization and applications of layered double hydroxides containing organic guests. New J. Chem. 105–115. https://doi.org/10.1039/A708319J

O'Loughlin, E.J., Kelly, S.D., Cook, R.E., Csencsits, R., Kemner, K.M., 2003. Reduction of uranium(VI) by mixed iron(II)/iron(III) hydroxide (green rust): Formation of UO2 nanoparticles. Environ. Sci. Technol. 37, 721–727. https://doi.org/10.1021/es0208409

Pan, Y.-H., Sader, K., Powell, J.J., Bleloch, A., Gass, M., Trinick, J., Warley, A., Li, A., Brydson, R., Brown, A., 2009. 3D morphology of the human hepatic ferritin mineral core: New evidence for a subunit structure revealed by single particle analysis of HAADF-STEM images. J. Struct. Biol. 166, 22–31. https://doi.org/10.1016/j.jsb.2008.12.001

Pan, Y., Brown, A., Brydson, R., Warley, A., Li, A., Powell, J., 2006. Electron beam damage studies of synthetic 6-line ferrihydrite and ferritin molecule cores within a human liver biopsy. Micron 37, 403–411. https://doi.org/10.1016/j.micron.2005.12.009

Pan, Y.H., Vaughan, G., Brydson, R., Bleloch, A., Gass, M., Sader, K., Brown, A., 2010. Electron-beam-induced reduction of Fe3+ in iron phosphate dihydrate, ferrihydrite, haemosiderin and ferritin as revealed by electron energy-loss spectroscopy. Ultramicroscopy 110, 1020–1032. https://doi.org/10.1016/j.ultramic.2010.01.008

Paterson, J.H., Krivanek, O.L., 1990. Elnes of 3d transition metal oxides. Ultramicroscopy 32, 319–325.

Perez, J.P.H., Freeman, H.M., Schuessler, J.A., Benning, L.G., 2019. The interfacial reactivity of arsenic species with green rust sulfate (GRSO4). Sci. Total Environ. 648, 1161–1170. https://doi.org/10.1016/j.scitotenv.2018.08.163

Refait, P., Bon, C., Simon, L., Bourrié, G., Trolard, F., Bessière, J., Gènin, J.-M.R., 1999. Chemical composition and Gibbs standard free energy of formation of Fe(II)-Fe(III) hydroxysulphate green rust and Fe(II) hydroxide. Clay Miner. 34, 499–510.

Refait, P., Buaer, P., Olowe, A.A., Genin, J.M.., 1990. The substitution of Fe2+ ions by Ni2+ ions in the green rust compound studied by Mossbauer effect. Hyperfine Interact. 57, 2061–2066.

Refait, P., Simon, L., Génin, J.M.R., 2000. Reduction of SeO42- anions and anoxic formation of iron(II) - Iron(III) hydroxy-selenate green rust. Environ. Sci. Technol. 34, 819–825. https://doi.org/10.1021/es990376g

Sader, K., Schaffer, B., Vaughan, G., Brydson, R., Brown, A., Bleloch, A., 2010. Smart acquisition EELS. Ultramicroscopy 110, 998–1003. https://doi.org/10.1016/j.ultramic.2010.01.012

Shannon, R.D., 1976. Revised effective ionic radii and systematic studies of interatomic distances in halides and chalcogenides. Acta Crystallogr. Sect. A 32, 751–767. https://doi.org/10.1107/S0567739476001551

Simon, L., François, M., Refait, P., Renaudin, G., Lelaurain, M., Génin, J.M.R., 2003. Structure of the Fe(II-III) layered double hydroxysulphate green rust two from Rietveld analysis. Solid State Sci. 5, 327–334. https://doi.org/10.1016/S1293-2558(02)00019-5

Skovbjerg, L.L., Stipp, S.L.S., Utsunomiya, S., Ewing, R.C., 2006. The mechanisms of reduction of hexavalent chromium by green rust sodium sulphate: Formation of Cr-goethite. Geochim. Cosmochim. Acta 70, 3582–3592. https://doi.org/10.1016/j.gca.2006.02.017

Sumoondur, A., Shaw, S., Ahmed, I., Benning, L.G., 2008. Green rust as a precursor for magnetite: an in situ synchrotron based study. Mineral. Mag. 72, 201–204. https://doi.org/10.1180/minmag.2008.072.1.201

Thomas, A.N., Eiche, E., Göttlicher, J., Steininger, R., Benning, L.G., Freeman, H.M., Dideriksen, K., Neumann, T., 2018. Products of Hexavalent Chromium Reduction by Green Rust Sodium Sulfate and Associated Reaction Mechanisms. Soil Syst. 2. https://doi.org/10.3390/soilsystems2040058

Usman, M., Byrne, J.M., Chaudhary, A., Orsetti, S., Hanna, K., Ruby, C., Kappler, A., Haderlein, S.B., 2018. Magnetite and Green Rust: Synthesis, Properties, and Environmental Applications of Mixed-Valent Iron Minerals. Chem. Rev. 118, 3251–3304. https://doi.org/10.1021/acs.chemrev.7b00224

Van Aken, P.A., Liebscher, B., 2002. Quantification of ferrous/ferric ratios in minerals: New evaluation schemes of Fe L23 electron energy-loss near-edge spectra. Phys. Chem. Miner. 29, 188–200. https://doi.org/10.1007/s00269-001-0222-6

Zhang, Y., Wei, S., Lin, Y., Fan, G., Li, F., 2018. Dispersing Metallic Platinum on Green Rust Enables Effective and Selective Hydrogenation of Carbonyl Group in Cinnamaldehyde. ACS Omega 3, 12778–12787. https://doi.org/10.1021/acsomega.8b02114
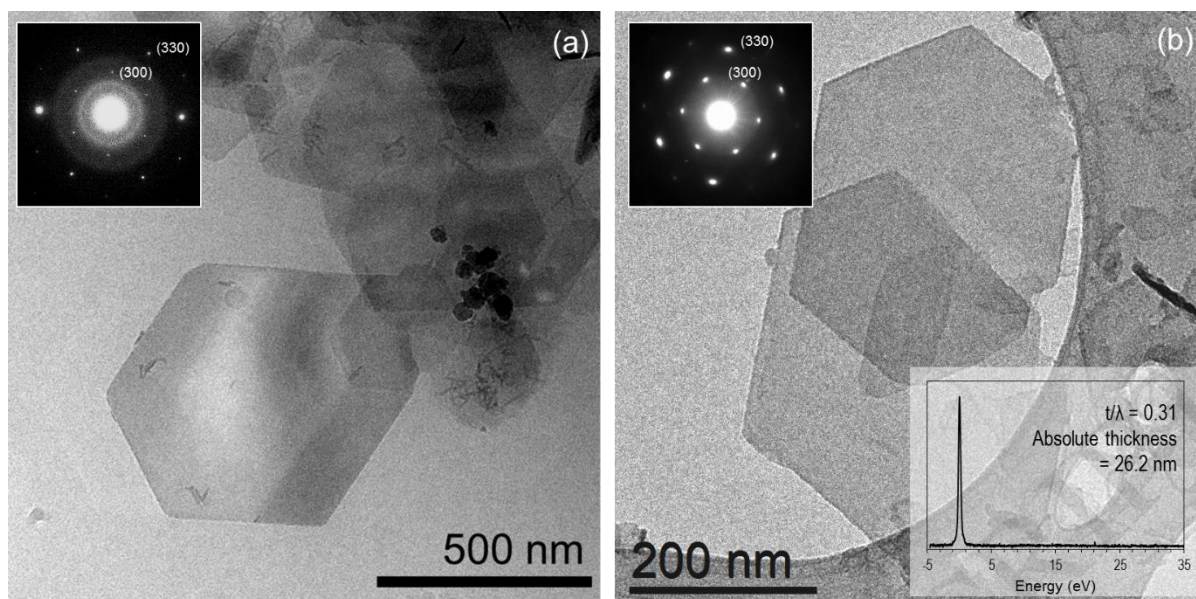
Figure 1 TEM images and SAED pattern (inset) of GR$_{SO4}$ (a) cryo frozen-hydrated sample preparation (b) anoxic drop-cast dry sample preparation. Note the additional amorphous ring in (a) from the scattering of electrons by ice. Dashed lines represent areas associated with the SAED pattern, and the low loss EELS spectrum for calculating specimen thickness is shown in (b).
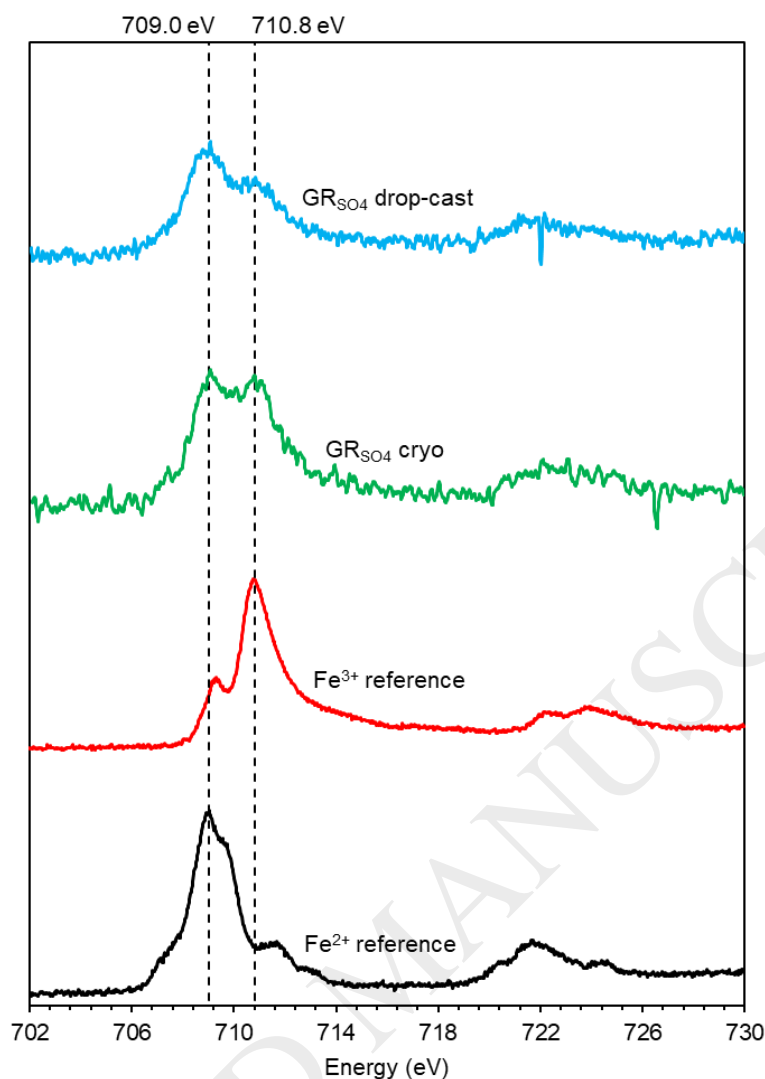
Figure 2. Background subtracted Fe L$_{3,2}$-edge spectra for Fe^{2+} (black) and Fe^{3+} (red), plus lowest fluence GR$_{SO4}$ Fe L$_{3,2}$-edge spectra from cryo (frozen hydrated suspension) sample preparation (green) at 255 e$^-$Å^{-2} and GR$_{SO4}$ from anoxic drop-cast sample preparation (blue) at 50 e$^-$Å^{-2}. Due to a low signal to noise ratio in the cryo spectrum (due to high levels of scattering in ice), a 5 point moving average has been applied to the data.
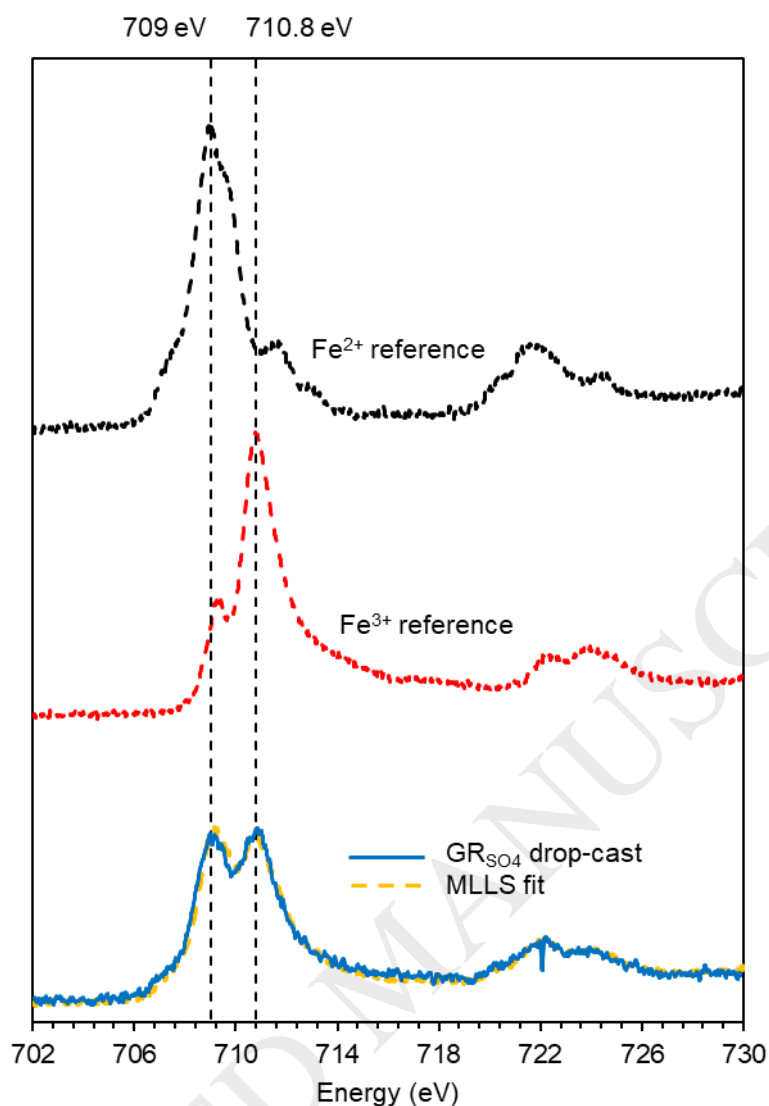
Figure 3. Example MLLS fitting of a background subtracted and area normalised Fe $L_{3,2}$-edge spectrum of anoxic drop-cast and dried GR_{SO4} (blue) fitted against a reference spectrum MLLS fit (yellow) from haematite (Fe^{3+}) (red) and hedenbergite (Fe^{2+}) (black). The estimated Fe(II)/Fe(III) ratio is 0.89 ± 0.09. Received fluence for GR_{SO4} spectrum is 730 $e^-Å^{-2}$.
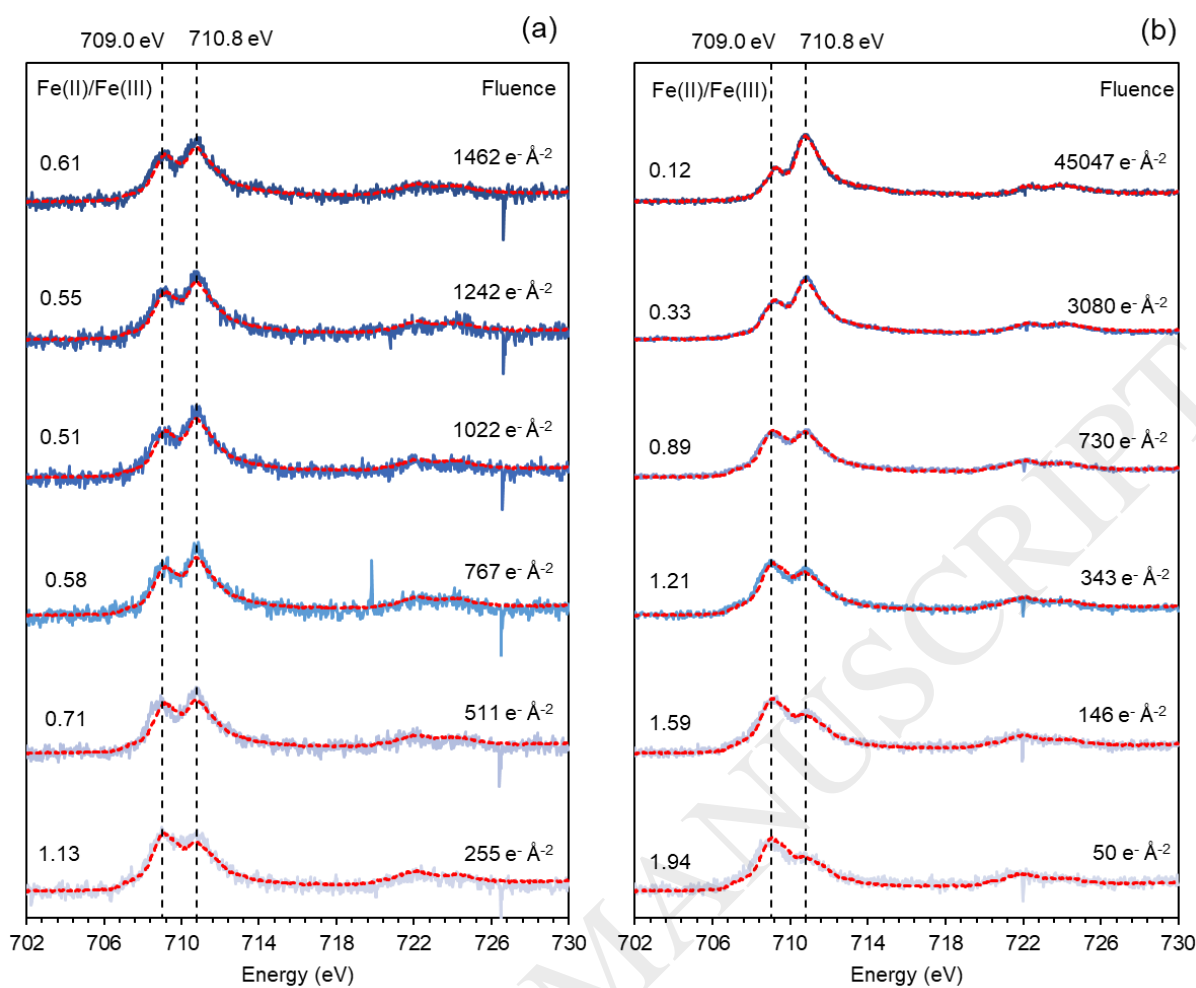
Figure 4 Stacked core loss EEL spectra (blue) showing changing shape of the Fe L₃ edge during electron irradiation in cryo-TEM (a) and anoxic drop-cast (b) sample preparation methods. The MLLS fits are shown in red. The corresponding Fe(II)/Fe(III) ratios are shown on the left hand side, and the associated electron fluence shown on the right hand side.
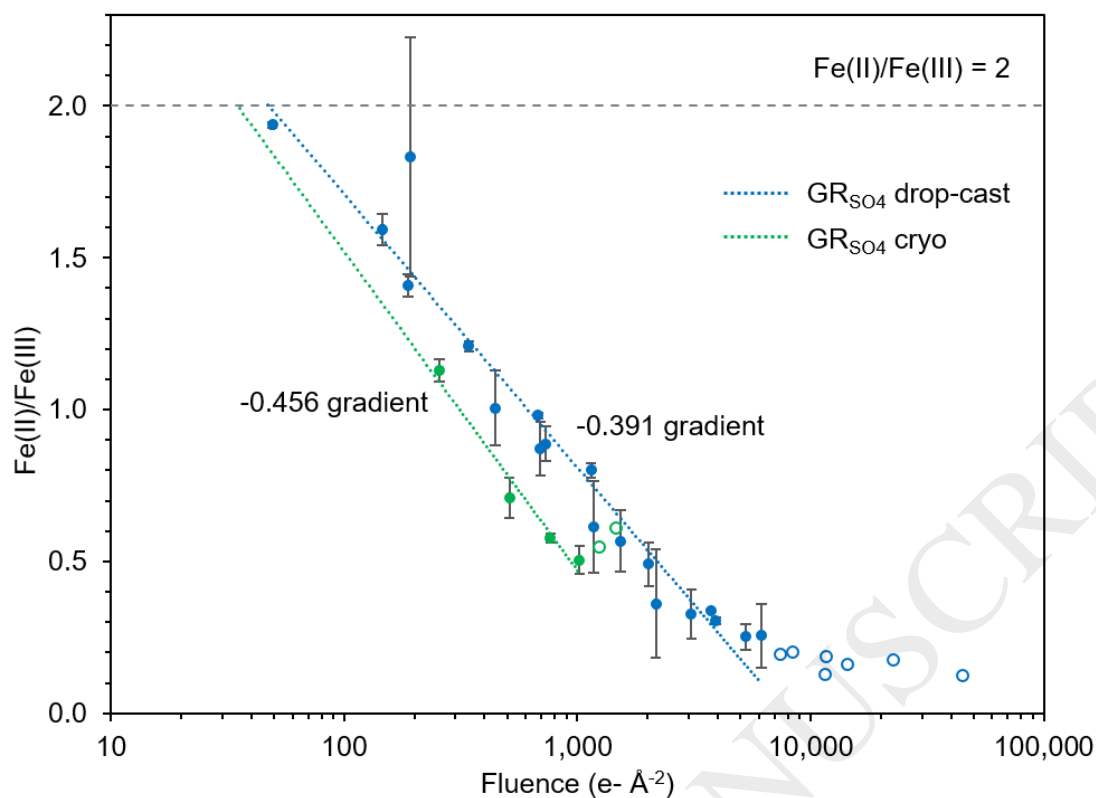
*Figure 5 Change in Fe(II)/Fe(III) content with electron fluence for conventional (anoxic drop-cast) sample preparation (blue) and cryo (frozen-hydrated) sample preparation (green). Logarithmic (dashed) trendlines have been extrapolated to Fe(II)/Fe(III)=2, terminating where data points begin to plateau at higher fluences (non-filled data points). The error in fluence is not shown here however we estimated a maximum variation of 12% due to a change in probe current during **in-situ** measurements. The error in Fe(II)/Fe(III) ratio was based on deviation from the least–squares trendline. Note that the cryo data is from a single GR plate whereas the plotted anoxic drop-cast data is from three different GR plates; this is due to the fact that in cryo-TEM it is more challenging to find a suitable sample area (i.e. enough specimen in a thin region of vitreous ice).*